Check for updates

RESEARCH ARTICLE

NANO · MICRO small
www.small-journal.com

Transmetalation for DNA-Based Molecular Electronics

Arpan De, Brandon Lu, Yoel P. Ohayon, Karol Woloszyn, William Livernois, Lara Perren, Chu-fan Yang, Chengde Mao, Antia S. Botana, Joshua Hihath, James W. Canary, Ruojie Sha, M.P. Anantram, and Simon Vecchioni**

The rational design of molecular electronics remains a grand challenge of materials science. DNA nanotechnology has offered unmatched control over molecular geometry, but direct electronic functionalization is a challenge. Here a generalized method is presented for tuning the local band structure of DNA using transmetalation in metal-mediated base pairs (mmDNA). A method is developed for time-resolved X-ray diffraction using self-assembling DNA crystals to establish the exchange of Ag^{+} and Hg^{2+} in T:T base pairs driven by pH exchange. Transmetalation is tracked over six reaction phases as crystal pH is changed from pH 8.0 to 11.0, and vice versa. A detailed computational analysis of the electronic configuration and transmission in the ensuing crystal structures is then performed. This findings reveal a high conductance contrast in the lowest unoccupied molecular orbitals (LUMO) as a result of metalation. The ability to exchange single transition metal ions as a result of environmental stimuli heralds a means of modulating the conductance of DNA-based molecular electronics. In this way, both theoretical and experimental basis are established by which mmDNA can be leveraged to build rewritable memory devices and nanoelectronics.

1. Introduction

The advent of DNA nanotechnology came from Ned Seeman's 1982 proposal of the self-assembling, three-dimensional (3D) crystal for the determination of biomolecular structures.[1] In 1987, Seeman and Robinson proposed the scaffolding of electronic moieties in such lattices for the development of nanoelectronics.[2] The evolution of DNA nanotechnology has seen remarkable progress in the ensuing four decades, aided in part by solid-phase synthesis techniques that obviated early synthetic challenges, and ever more complex modeling tools for structure design.[3–5] Complex two-dimensional (2D) tile motifs and crystals were developed, enabling the realization of programmable matter in solution and on surfaces.[6,7] Principles of computer science enabled the algorithmic self-assembly of aperiodic crystals from DNA Wang tiles, as well as the birth of DNA origami and meta-origami arrays.[8,9] DNA has further been used to demonstrate reconfigurable structures of varying complexity, including DNA tweezers, nanomechanical lattices, DNA walkers, DNA Möbius strips, and computation from DNA neural networks—all based on the reconfiguration of whole oligonucleotides.[10–15] Though such systems have been used for complex, thermodynamically-driven algorithms, this reconfigurability has not been leveraged toward dynamic switching in intrinsically-conductive electronic devices and systems, nor has reconfiguration been streamlined at the atomic level.

Significant attention has been paid to optical devices from nanoparticles or dyes,[16,17] and surface functionalization for photonic applications,[18] but band engineering in DNA materials to tune its electrical and optical properties has seen little progress. With the aggressive scaling of solid-state devices, DNA-based nanoelectronics as suggested by Seeman and Robinson presents a promising alternative to conventional lithography. The small geometry of DNA strands—0.34 nm nucleotide pitch, 2 nm diameter—is appealing for device implementation as this addressability resides at the state-of-the-art fabrication limits of commercial semiconductor devices.[19] Proposals have been made to use DNA to build resonant tunneling diodes and superlattices akin to those in conventional semiconductors.[20–25] We have previously shown that two DNA strands with comparable

A. De, W. Livernois, M. Anantram
Department of Electrical and Computer Engineering
University of Washington
Seattle, WA 98195, USA
E-mail: anantmp@uw.edu

B. Lu, Y. P. Ohayon, K. Woloszyn, L. Perren, C.-fan Yang, J. W. Canary, R. Sha, S. Vecchioni
Department of Chemistry
New York University
New York, NY 10003, USA
E-mail: sv1091@nyu.edu

C. Mao
Department of Chemistry
Phurdue University
West Lafayette, IN 47907, USA

A. S. Botana
Department of Physics
Arizona State University
Tempe, AZ 85281, USA

J. Hihath
Center for Bioelectronics and Biosensors
School of Electrical
Computer and Energy Engineering
Arizona State University
Tempe, AZ 85287, USA

The ORCID identification number(s) for the author(s) of this article can be found under https://doi.org/10.1002/smll.202411518

DOI: 10.1002/smll.202411518

 © 2025 Wiley-VCH GmbH

lengths can have nearly two orders of magnitude difference in conductance, leading to proposals for read-only memory (ROM) based on assembling DNA into 2D and 3D crossbars.[26,27]

Although progress has been made in electrically characterizing DNA, the fundamental bottleneck in experimentally realizing state-of-the-art comparable electronic behavior is the large bandgap of DNA (3–4 eV), weak electronic coupling between stacked bases, and the lack of doping strategies to tune the Fermi energy—all of which lead to low electrical conductivity. Recent proposals to increase the electrical conductivity include structural transformation from B- to A-form,[28] twisting and stretching of DNA,[29] modifying the base stacking via organic molecule intercalation,[30] and base pair modification by redox reactions.[31] An alternate strategy to modify DNA for electronic and optical properties involves the metalation using nanoparticles or thin films that disperse across the surface of the double helix, which is a powerful nanometer-scale design tool but lacks the isomorphism essential for electronic devices.[32–36] Specifically, interactions between metal ions and DNA have been widely explored in the past five decades. As early as 1952, Katz observed an interaction between Hg^{2+} and nucleic acids extracted from calf thymus.[37] In 1993, Gao et al performed crystallographic studies that elucidated the diverse binding modes of Co^{2+}, Cu^{2+}, and Ba^{2+} to Z-DNA.[38] Subsequently, in 1999, Aich et al. developed a molecular wire by intercalating divalent metals into DNA in alkaline environments.[39] Following up, in 2003, Tanaka et al built a magnetic chain leveraging ferromagnetic coupling between Cu^{2+} mediated adjacent base pairs.[40] A notable strategy to modify DNA emerged from the work of Miyake et al, where they showed specificity of Hg^{2+} ion binding to T:T mismatched base pairs in dsDNA, with stability tested across a wide pH spectrum (3.0 to 11.0).[41] Similarly, Ono et al demonstrated the specificity of Ag^{+} ions in C:C base pairs.[42] Reveguk et al further explored the impact of metal binding to cytosine chains at low (5.5) and high (9.0) utilizing steady state as well as time-resolved fluorescence and absorption methods.[43] They found that the average fluorescence lifetime increases considerably at low pH. Schmidt et al investigated the kinetics of metal binding to mismatched base pairs, observing that T-Hg^{2+}-T complexes exhibit notable stability due to their low dissociation constants, potentially enabling the construction of stable single-molecule electronics.[44] Furthermore, Bethur et al have demonstrated the formation of stable Ag^{+}-mediated G-duplex.[45] However, all these studies are more focused on expanding the versatility of nucleic acid and not on building electronic devices. More importantly, none of these studies demonstrate reconfigurability or transmetalation.

To this end, we recently demonstrated, using self-assembled DNA crystals,[46] that the structures of mmDNA base pairs could be swiftly and reliably solved in a variety of aqueous conditions, and further showed the effect of metalation on the bandgap of the surrounding DNA chain.[47] Specifically, we demonstrated a pH-based titration effect in T:T base pairs, in which competition between Ag^{+} and Hg^{2+} caused homo- and heterobimetallic metal base pairs. At neutral pH (8.0), two Hg^{2+} ions bind to form a homobimetallic (two identical metal ions) base pair; while at slightly alkaline pH (9.5), a mixed, heterobimetallic (two different metal ions) Ag^{+}/Hg^{2+} base pair forms; and finally at high pH (11.0), two Ag^{+} ions dominate.[48] The base pairs further change from mononuclear to dinuclear pairs, depending on the choice of Tris or MOPS buffers. This result suggested a means both of conductance modulation by pH change, as well as the possibility of reconfigurable electronics based on DNA-based transmetalation between Ag^{+} and Hg^{2+}. This metalation technique provides a means of moving single atoms in response to environmental stimuli as an alternative to thin films and particles, and it overcomes the conductance bottleneck by direct injection of states into the bandgap of DNA.

In this study, we develop a crystallographic method to capture structural intermediates in DNA-based transmetalation, effectively capturing the "structure" of a nearly-reversible chemical reaction. We further theoretically model silver- and mercury-doped DNA at a variety of pH values to show that while the HOMO levels primarily reside on the base pairs, the LUMO levels are significantly influenced by the metal atoms. We calculate the conductance of crystallographically derived mmDNA and provide insight into the conductance contrast theoretically possible in such a system. The reversibility of metal atom intercalation and the accompanying conductance contrast offer promise for bio-electronic memory research and rewritable memory elements.

2. Results

2.1. Experimental and Theoretical Overview

The predictable behavior of metal coordination at varying pH points asserts the reconfigurability of Ag^{+} and Hg^{2+} ions between thymine bases as pH changes. To investigate the reconfigurability of mmDNA base pairs and to carry out the ensuing electronic fingerprinting, we employ the tensegrity triangle, a DNA motif that readily self-assembles into 3D crystals in programmable space groups;[49,50] here we employ a motif that consistently yields space group R3.[51–53] These crystals are amenable to X-ray diffraction and have been used to solve the biomolecular structure of mmDNA base pairs in various configurations.[48] Here, we self-assemble DNA tensegrity triangles with T:T base pairs in the presence of both Ag^{+} and Hg^{2+} and solve the structures of the mmDNA pairs undergoing pH-based reconfiguration (**Figure 1a–c**). We then consider the most critical region in crystal structures generated from the tensegrity triangle, which includes the seven base pair (bp) regions surrounding the metal ion, to understand the ensuing charge transport properties (Figure 1d). After partial optimization of the structure using density functional theory (DFT), the Hamiltonian is obtained along with the energy levels. This Hamiltonian is used to calculate the transport properties using the Green's function approach.[30,54] Subsequently, the transmission profile, conductance, and density of states are computed. All experimental and simulation methods are discussed in Sections S(1–4) (Supporting Information).

2.2. Time-Resolved Crystallography and Reconfiguration

To test the metal exchange processes, we performed time-resolved crystallography of pH exchange by flash-freezing crystals in liquid nitrogen after a significant pH change at specific

© 2025 Wiley-VCH GmbH

16136829, 0, Downloaded from https://onlinelibrary.wiley.com/doi/10.1002/smll.202411518 by University Of Washington, Wiley Online Library on [14/05/2025]. See the Terms and Conditions (https://onlinelibrary.wiley.com/terms-and-conditions) on Wiley Online Library for rules of use; OA articles are governed by the applicable Creative Commons License

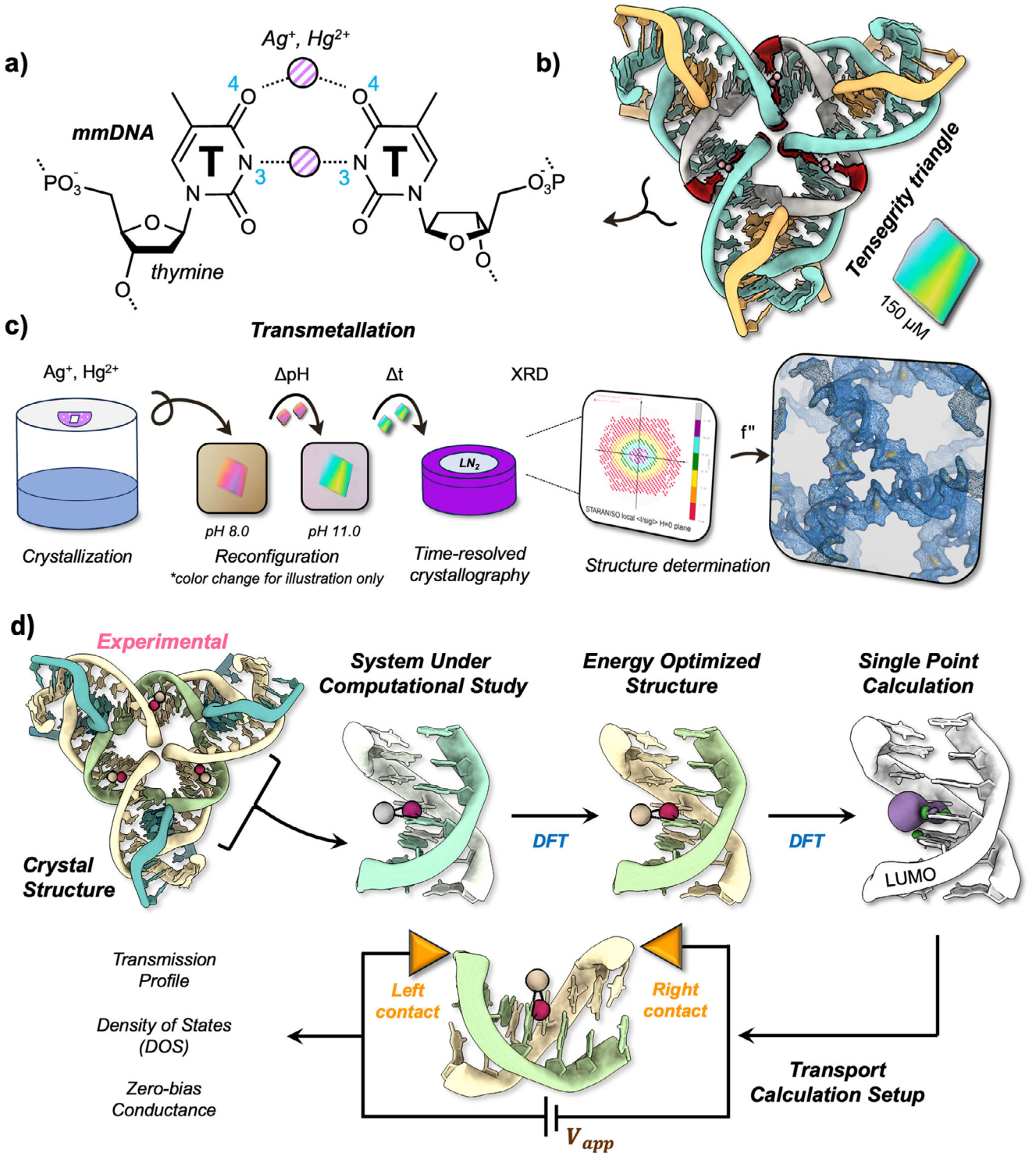


Figure 1. Metal-mediated DNA a) T-T base pairs bind Ag^{+} and Hg^{2+} in dinuclear conformations at different pH values. The N3 and O4 positions are annotated, blue. N3-metal bonds are known to be strong, linear coordination bonds, while O4-metal bonds are weaker and more fluid. b) Tensegrity triangles are designed with one T-T mmDNA pair per edge (red) and self-assemble into macroscopic crystals of diffraction quality (inset). c) Reconfiguration scheme is shown. Crystals are first grown at pH extrema (8.5, 11.0), then cryoprotected in buffers of different pH (crystal colors here are schematic, not indicative of real color change). The crystals are soaked at the new pH from 5–300 s and then flash frozen in liquid nitrogen to capture the reaction intermediate. Structure determination is carried out with f'' refinement to quantify the metal occupancy and identity at each time point. d) Computational setup: step1: mmDNA structure extracted from the DNA tensegrity triangle; step2: the structure is cut to consider the 7 bp region surrounding the metal; step3: the structure is DFT optimized; step4: DFT calculations are performed on optimized structures; and step5: transport calculations are carried out.

© 2025 Wiley-VCH GmbH

16136829, 0, Downloaded from https://onlinelibrary.wiley.com/doi/10.1002/smll.202411518 by University Of Washington, Wiley Online Library on [14/05/2025]. See the Terms and Conditions (https://onlinelibrary.wiley.com/terms-and-conditions) on Wiley Online Library for rules of use; OA articles are governed by the applicable Creative Commons License

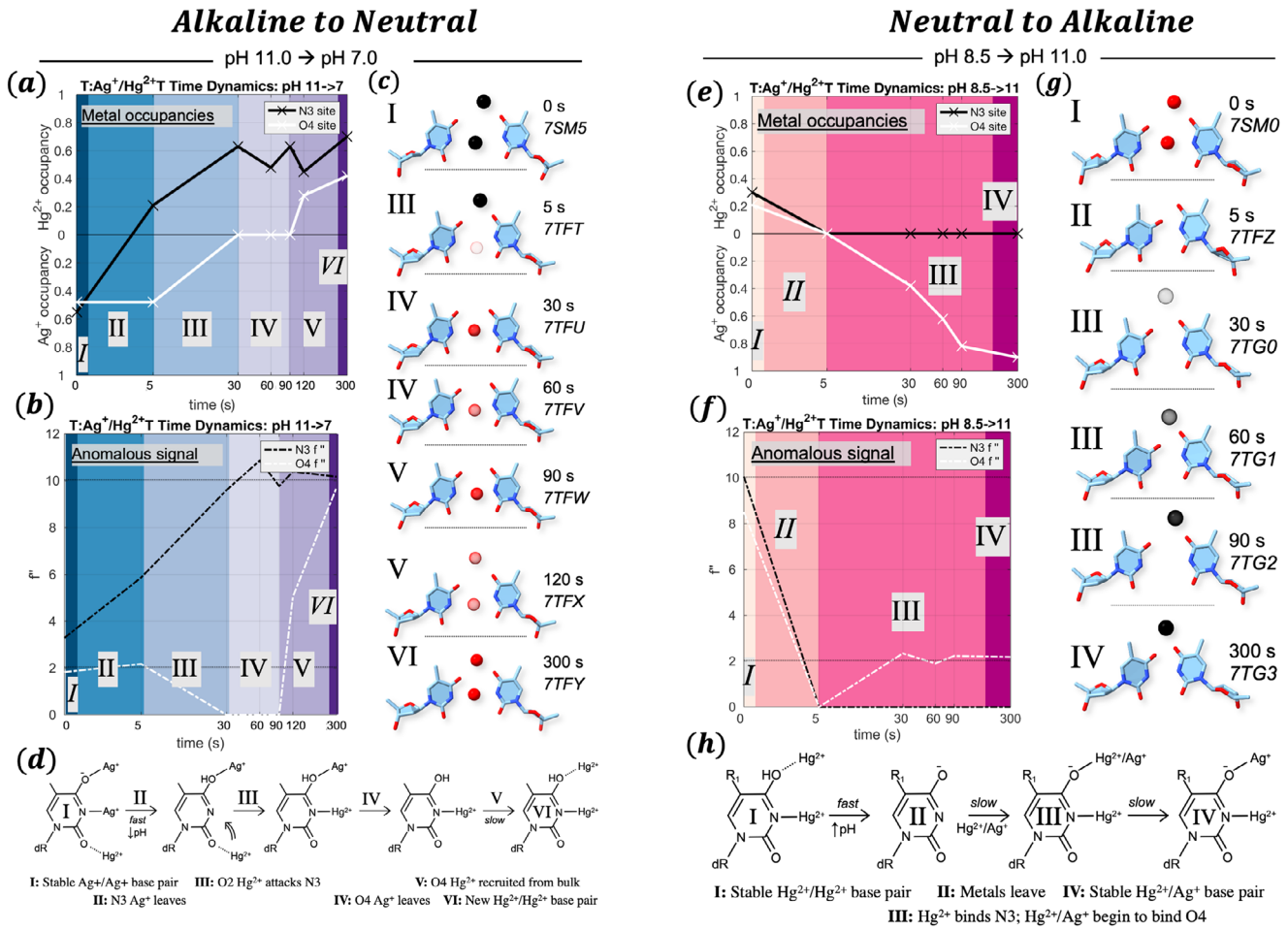


Figure 2. Transmetalation: Time-resolved crystallography of transmetalation reactions in dT:Hg^{2+}/Ag^{+}:dT as pH was decreased from 11.0 to 7.0 (left column) and increased from 8.5 to 11 (right column). All ions are recruited locally from within the crystal. a,e) Metal occupancy at N3 and O4 sites for Hg^{2+} are plotted on the positive y axis and occupancy of Ag^{+} on negative y axis over log-scaled time. These reactions are articulated over six (left) and four (right) distinct phases. Shape of occupancy curves roughly matches (b,f) f′′ plots of each site over log time. Horizontal dotted lines show calculated Hg^{2+} and Ag^{+} f′′ at 12307 eV (10.17 and 2.06, respectively). c,g) Crystal structure shown at each time point, with transparency of ions (Hg^{2+}: red spheres; Ag^{+}: black spheres) set to the normalized occupancy at each site. Time before quenching in liquid nitrogen and PDB ID are indicated for each structure. d,h) A reaction scheme for the pH-based transmetalation is proposed.

time points, thereby quenching the atomic displacement reactions (Figure 1c). Crystals were grown in the presence of both Ag^{+} and Hg^{2+} at each pH boundary (8.5 and 11.0) and immersed in the buffer with reversed pH values (11.0 and 7.0, respectively). pH 7.0 was chosen to increase the occupancy of Hg^{2+} during the transmetalation reaction and improve quantification of reaction progress, as we have previously seen relatively low occupancy at pH 8.5. Transmetalation reactions, when pH changes from alkaline (11.0) to neutral (7.0) and from neutral (8.5) to alkaline (11), are shown in **Figure** 2a–d and 2e-h, respectively. Heavy atoms were characterized through f′′ refinement (Tables S2-S3, Supporting Information) as established previously.[47] In brief, the anomalous scattering signal coming from metal ions is calibrated to the collection wavelength, allowing the occupancy of Ag^{+} and Hg^{2+} to be quantitatively derived from the data. By first solving, and then fixing the X, Y, and Z coordinates and B factors of the molecule, we can identify the occupancy (Q factor) from the known f′′ of a fully occupied metal at the collection energy. The occupancy and f′′ relationship are plotted in Figure 2 across the reaction snapshots. We find that the tensegrity triangle allows for atomistic levels of detail when it comes to heavy atom position, enabling the measurement of a ≈4 Å atomic motion in these atomic displacement reactions.

Crystals grown at pH 11.0 and immersed in pH 7.0 cryoprotectant are diffracted to resolutions between 3.9 and 5.0 Å (occupancies and anomalous signal can be found in Figure 2a,b, Table S2 (Supporting Information); structures can be found in Figure 2c. We observed that the metals are coordinated at the N3 position, where protonation of thymine occurs. It immediately switches from Ag^{+} to Hg^{2+} upon pH exchange and remains Hg^{2+} thereafter. In comparison, the O4 position contains Ag^{+} at 5s, then loses its bound metal until finally switching to Hg^{2+} 120 s after starting the reaction. These states can be seen in the proposed reaction scheme (Figure 2d). The difference in the transition time of the N3 position and the O4 position between these two datasets reinforces the hypothesis that Ag^{+} binds comparatively weakly at

© 2025 Wiley-VCH GmbH

16136829, 0, Downloaded from https://onlinelibrary.wiley.com/doi/10.1002/smll.202411518 by University Of Washington, Wiley Online Library on [14/05/2025]. See the Terms and Conditions (https://onlinelibrary.wiley.com/terms-and-conditions) on Wiley Online Library for rules of use; OA articles are governed by the applicable Creative Commons License

pH 11.0 to N3 compared to Hg^{2+} binding to N3 at neutral pH levels. This affinity difference appears to outweigh the impact of greater accessibility of the O4 site to solvent ions in this experiment.

The crystals grown at pH 8.5 and immersed in buffered cryoprotectant solution at pH 11.0 were diffracted to resolutions between 4.4 and 6.1 Å (occupancies and anomalous signal can be found in Figure 2e,f, Table S3 (Supporting Information); structures can be found in Figure 2g; proposed reaction scheme in Figure 2h. In these data, we observed that the N3 position did not always contain any metal after pH change, which shows that at pH 11.0, the ability of the N3 position to bind Hg^{2+} sharply decreases. However, we do not observe Ag^{+} binding, which indicates that Ag^{+} binds very slowly in the N3 position and requires a much longer timescale to observe, or is not regenerated in these buffer conditions. In contrast, a high occupancy Ag^{+} appears in the O4 position after the 60 s, with occupancy increasing over time. This may be due to the increased accessibility of the major groove O4 position to the surrounding solvent compared to the solvent-protected N3 site. The absence of N3 Ag^{+} regeneration could also indicate that the major groove, O4 Ag^{+} presents a diffusion barrier to regenerating the dinuclear Ag^{+} base pair. These states can be seen in the proposed reaction scheme (Figure 2d).

The data also contained instances of heavy atoms with f′′ values that are in between the theoretical values of silver (2.06) and mercury (10.17) at 12307 eV.[55] These metal sites were refined to have the best agreement with $2F_o$-F_c and F_o-F_c electron density maps. Specific information on ambiguous sites can be found in Section S1.6 (Supporting Information). We emphasize that these sites are ambiguous and cannot be characterized as only Hg^{2+} or Ag^{+} and contain significant contributions from both metals. As such, we posit that these molecular structures contain Hg^{2+} within some crystallographic unit cells and Ag^{+} in others as an intermediate in the slow atomic displacement reaction. Despite the much longer timescales, our process is similar to time-dependent crystallography, which has been used to determine reaction dynamics and intermediates.[56,57] We anticipate that future studies can leverage these results to investigate the mechanistic details of mmDNA reactions.[58,59] Overall, we have shown two available, solvent-accessible, and programmable sites on thymine that freely interact with environmental Hg^{2+} and Ag^{+} with distinct characteristics.

2.3. Conductance Analysis of mmDNA Structures

To study the effect of metal ion placement and identity on the viability of mmDNA-based molecular electronics, ten DNA structures from tensegrity triangles are considered with environmental pH ranging from 7.0–11.0 as reported here and previously.[48] Band gaps are generated in **Figure 3**. Structures with a single metal ion (see Figure 2c-IV, Figure 2g-VI) are modeled in **Figure 4**, while dinuclear base pairs are considered in **Figure 5**. These specific two metal base pairs were chosen to reflect the start and end points of transmetalation from low pH (8.5) to high pH (11.0). Pristine DNA without metalation is analyzed at low (7.0–9.0) and high (10.0–11.0) pH to provide a baseline and is constructed by removing a metal ion from a mmDNA structure. A previous structure of a pristine T–T pair is isomorphic at neutral pH.[47] The simulation methodology is detailed in Section S4.1 (Supporting Information).

For a comprehensive understanding of the impact of metal coordination, we have considered three categories of conformations: i) single metal coordinated (PDB IDs: 7SLG, 7TG6) ii) dinuclear coordinated (PDB IDs: 7SM0, 7SM1,7SM2,7SM3,7SM4,7SM5) and iii) non-metalated. When the pH is elevated from low (7.0–9.0) to high (10.0–11.0), all canonical A-T base pairs lose the H3 hydrogen attached to the N3 site of all thymines due to its pKa value (see Figure 3a). In metalated motifs at low pH, mismatched thymine base pairs tend to adopt the *enol* configuration to accommodate the metal atom. This causes the H3 hydrogens to move toward the O4 sites as depicted in Figure 3b.[47] At high pH, where the T-T base pair lacks H3 hydrogens, the metal can coordinate with the bases (Figure 3c). Since pH controls the protonation state of the thymine nucleobase (pKa of 9.7), we consider both fully protonated and deprotonated structures from pH values between 9.0 and 10.0. The sequence under study contains five thymine nucleobases (including the T–T mismatch); therefore, we have removed five H3 hydrogens to represent the deprotonated states.

We have examined the bandgaps of all the metalated and non-metalated motifs with definite protonated or deprotonated states in Figure 3d. The bandgaps of the pristine structures at neutral and high pH are calculated at 4.12 and 3.80 eV, respectively ('No metal' of Figure 3d), matching expected values from previous studies.[47] Metal ion coordination—N3-Hg^{2+} at pH 7.0, and O4-Ag^{+} at pH 11.0—leads to the addition of new LUMO levels, which causes the bandgap to shrink as shown in 'Single metal' of Figure 3d. The corresponding LUMO values are listed in Table S6 (Supporting Information). When a single ion is bound, the bandgap shrinks by 13.8% (0.57 eV) for Hg^{2+} and 31.1% (1.18 eV) for Ag^{+}. This state is achieved experimentally as the stable structure of T:T mismatches in MOPS buffer when presented with a single metal ion species, as well as a reaction intermediate (see Figure 2c-IV,g-V).[47,60]

By contrast, the choice of Tris buffer enables the dinuclear states reported here (Figure 2) and previously,[48] highlighting the effects of solvation on metal speciation, and further on the high solvent-accessibility of the secondary O4 site in the major groove of DNA. This two-metal coordination leads to a bandgap shrinkage of 52.7% (1.95 eV) and 44.7% (2.10 eV) for Hg^{2+} and Ag^{+} respectively as depicted in the 'Double metals' of Figure 3d. From the bandgap variation in all the motifs, we can note three interesting trends: first, in non-metalated and single metal motifs the bandgap reduces in alkaline pH, while it remains comparable in double metal cases (≈0.15 eV difference between pH 8.5 and 11.0 in dinuclear coordinated motifs). Second, the change in bandgap between the initial (7.0 in single metal motifs and 8.5 in double metal motifs) and final pH (11.0 in all motifs), is highest in single metalated motifs, indicating that the charge transport in single metalated motifs is more sensitive toward nature of coordinated metal. Finally, moving left to right in Figure 3d reveals that a higher number of metal coordination leads to a lower bandgap at both low and high pHs, which is a promising lead for developing metalated DNA-based electronics.

At intermediate pH values, the bandgap modulation is determined by the metal ion locations and heterometallic coordination (Figure 3e). For every pH level in Figure 3e, we observe that the

© 2025 Wiley-VCH GmbH

16136829, 0, Downloaded from https://onlinelibrary.wiley.com/doi/10.1002/smll.202411518 by University Of Washington, Wiley Online Library on [14/05/2025]. See the Terms and Conditions (https://onlinelibrary.wiley.com/terms-and-conditions) on Wiley Online Library for rules of use; OA articles are governed by the applicable Creative Commons License

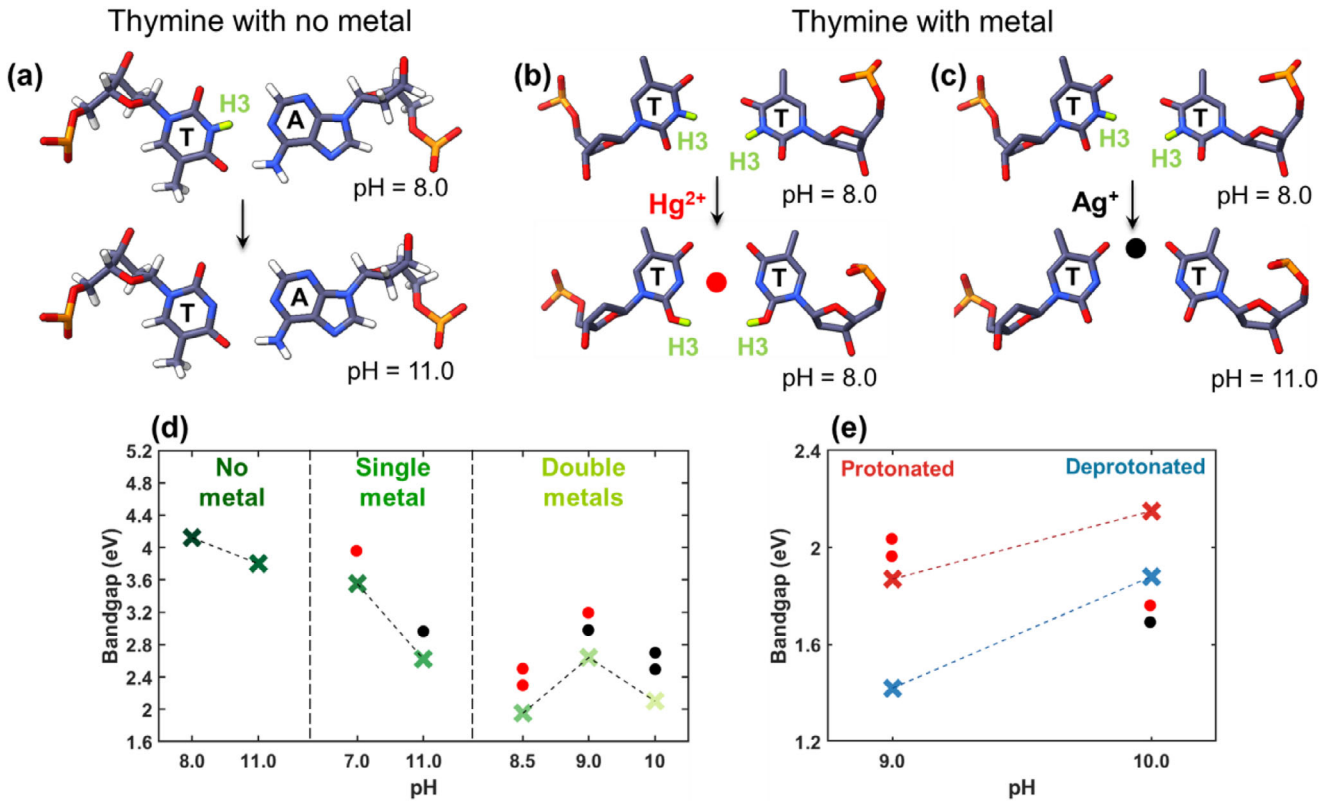


Figure 3. Band calculation for different DNA structures exhibiting the impact of metal coordination on the DNA bandgap. To perform DFT calculation for motifs at low (7.0–9.0) and high (10.0–11.0) pH, we have considered the protonation and deprotonation states of thymine as shown in (a-c). Thymine without metal a) loses the H3 hydrogen bounded to N3 site at high pH (> 10.0). However, due to metal coordination at low pH (< 9.0), mismatch T–T base pair results in shift of H3 hydrogen to O4 site. b); while that at high pH results in removal of those hydrogens from all thymine locations c). Bandgaps of motifs at (pH < 9.0 and pH > 10.0) are shown in d) that includes no metal, single and double metal coordination with Hg^{2+} (red circle) and Ag^{+} (black circle). At intermediate pH 9.0 and 10.0, two structures of the same mmDNA system have been considered to reflect the protonated and deprotonated cases near the pKa of thymine (pH 9.7). It is to be noted that presence and absence of H3 hydrogens are termed as protonated and deprotonated respectively. (a)-(c) show only the fourth base pair but the calculations in (d) and (e) are for the seven base pair calculations.

bandgap is reduced in the deprotonated state in comparison to the protonated one. Due to the removal of N3 hydrogens, a large shift in occupied energies between protonated and deprotonated states is seen: 0.75 and 0.59 eV at pH 9.0 and 10.0, respectively. Although bandgap shrinkage is indicative of enhanced conductance, a quantitative estimate of increased conductance can be done only by carrying out transport calculations.

We first investigate the effect of single metal coordination on conductance, using T:Hg^{2+}:T and T:Ag^{+}:T base pairs (Figure 4 top and bottom panels, respectively). The impact of metal atoms in modulating charge transport hinges on two factors apart from the metal type, namely, i) the charge of the metal and ii) their relative spatial position with respect to the atoms in the base pair. In Figure 4a, we notice that Hg^{2+} is positioned almost centrally within the T–T base pair with mean distances of 2.48 and 2.40 Å from the O4 and N3 sites. In contrast, Ag^{+} in Figure 4b, is at an average distance of 2.20 and 4.40 Å from the O4 and N3 sites respectively. Therefore, the charge transfer can be considered to mainly prevail between N3/Hg and O4/Ag in the top and bottom panels of Figure 4, respectively, leading to a reduction in the partial charges of the metal atoms (Hg^{2+}: 1.48 & Ag^{+}: 0.73). As a result, we notice a difference in the LUMO and LUMO+1 orbital maps for Hg^{2+} and Ag^{+} coordination as shown in Figure 4a,b respectively. While the lowest unoccupied orbital in the Hg^{2+} coordinated motif is localized on the metal/metalated base pair, in the Ag^{+} coordinated case, it is found on a non-metalated base pair. The reason can be attributed to the significantly reduced partial charge of Ag^{+}. We posit that the proximity of Ag^{+} with one of the O4 atoms (1.85 Å) facilitates strong conjugation, resulting in considerable electron transfer from O4 to Ag. Consequently, the available density of states in Ag is reduced, causing the LUMO to be on the DNA. To corroborate this hypothesis, we investigated the Ag^{+} coordinated motif by replacing Ag^{+} with Hg^{2+} as shown in Figure S4 (Supporting Information). We calculated the partial charge on Hg^{2+} to be 1.61 and observed the LUMO shifting back to the metal while LUMO+1 was on the DNA. For completeness, we have replaced Hg^{2+} in Figure 4 top panel with Ag^{+}, as demonstrated in Figure S5 (Supporting Information). The partial charge of silver further decreased to 0.59 due to increased conjugation with additional atoms, resulting in both LUMO and LUMO+1 residing on the DNA. Additionally, silver coordination leads to a LUMO peak near the conduction band edge (−0.91 eV), while mercury adds a LUMO peak deeper within the bandgap (−1.51 eV) when compared to the baseline case. On the other

© 2025 Wiley-VCH GmbH

16136829, 0, Downloaded from https://onlinelibrary.wiley.com/doi/10.1002/smll.202411518 by University Of Washington, Wiley Online Library on [14/05/2025]. See the Terms and Conditions (https://onlinelibrary.wiley.com/terms-and-conditions) on Wiley Online Library for rules of use; OA articles are governed by the applicable Creative Commons License

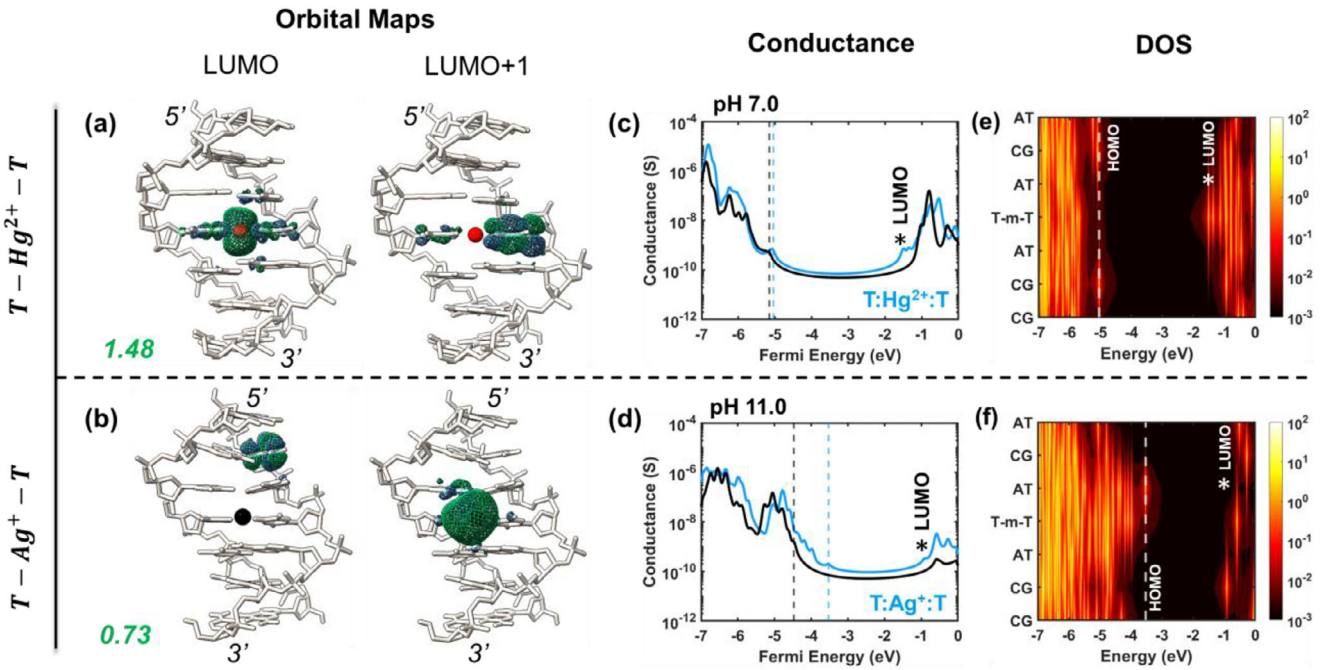


Figure 4. Single metal results: mmDNA with (top row) Hg^{2+} and (bottom row) Ag^{+} coordination. Corresponding LUMO & LUMO+1 orbital maps are shown in a) and b), respectively. Wavefunctions with absolute value larger than 0.02 are shown. Conductance variation with Fermi energy is plotted c) for Hg^{2+} and d) for Ag^{+} coordination. Density of states (DOS) for both structures are in (e) and (f). In (a, b), the numbers at bottom left corner in green color represent partial charge on the metal. The black lines in (c, d) show no-metal cases. In the DOS plots e, f), the white dotted line represents the corresponding HOMO energies.

hand, after coordination, the HOMO orbital continues to be primarily located on the nucleobases. While Hg^{2+} coordination changes the HOMO peak by 0.11 eV, the coordination of Ag^{+} causes a more substantial change by 0.90 eV.

To characterize the conductance changes, a useful figure of merit is the conductance contrast, or the ratio of conductance in the metalated and unfilled T:T base pair. In the single-metal atom case, the conductance contrast is 3.22 and 6.47 for Ag^{+} and Hg^{2+} coordinated base pairs, respectively, when the Fermi energy is set at LUMO. Overall, the density of states (DOS) is large at the metal base pair site (Figure 4e,f) when compared to non-metalated motifs (see Figure S6, Supporting Information) and is therefore directly responsible for the increased conduction. Figure S6 (Supporting Information) illustrates the universality of this feature for all cases. When the Fermi energy is close to HOMO or LUMO, conduction is higher in T:Hg^{2+}:T than T:Ag^{+}:T. The reason can be attributed to the combined effects of higher charge and coordination site of Hg^{2+} compared to Ag^{+} as seen in Figure 2a,b and Figure 4a,b. Furthermore, the difference between the HOMO and HOMO-1 energy levels for Ag^{+} and Hg^{2+} base pairs are 0.45 and 0.05 eV respectively. The small energy level separation in the case of Hg^{2+} helps enhance transmission across the duplex.

Increasing the concentration of metal ions or the buffer composition can lead to the coordination of two ions to form a dinuclear mmDNA base pair. The composition of the T–T base pair containing metal ions is shown in Figure 5, first row, derived from static experiments in crystals grown at a particular pH.[48] The stable configuration at pH 8.5 is a homobimetallic, Hg^{2+}/Hg^{2+} base pair. But as pH is increased to 10.0, the O4 Hg^{2+} is replaced by Ag^{+}. Further, an increase to pH 11.0 leads to the coordination of two Ag^{+} atoms. These states correspond to the alkaline-to-neutral transitions observed in Figure 2c, and to a lesser extent the neutral to alkaline dynamics in Figure 2g. Computationally we find that the number of unoccupied peaks in the bandgap is larger in the case of dinuclear coordination compared to single metal coordination, and the lowest two unoccupied peaks for homobimetallic Ag^{+}/Ag^{+} coordination are at −2.11 and −1.22 eV, while that for homobimetallic Hg^{2+}/Hg^{2+} are at −3.05 and −2.58 eV. The two lowest unoccupied molecular orbitals are shown in Figure 5 for each case. These orbitals are primarily at the metal atoms and correspond to the peaks in the bandgap in the conduction plots (see Figure 5 second row). From the orbital distributions at the lowest unoccupied orbital in the third row, we note that Hg^{2+} causes the LUMO to be broadened over N3 and O4 metals whether hetero- or homobimetallic but dinuclear Ag^{+} coordination results in localization over only O4-metal. This observation is consistent with the partial charge analysis (see third and fourth rows in Figure 5). We found that the partial charges of metals coordinated to O4 are consistently higher than those coordinated to N3 in homobimetallic motifs (pH 8.5 and 11.0). Correspondingly, the wavefunction at the lowest unoccupied orbital is more localized on the metal at O4 coordination sites. With respect to the heterobimetallic motifs (pH 10.0), in the fully protonated state (Figure 5b), the LUMO orbitals are well-broadened over both N3- and O4-coordinated metals, while in the deprotonated state (Figure 5c), the LUMO orbital is predominantly localized over the O4-coordinated Ag^{+}. In the deprotonated state, the loss of hydrogens from the thymines increases the negative charge of the DNA, leading to a reduc-

© 2025 Wiley-VCH GmbH

16136829, 0, Downloaded from https://onlinelibrary.wiley.com/doi/10.1002/smll.202411518 by University Of Washington, Wiley Online Library on [14/05/2025]. See the Terms and Conditions (https://onlinelibrary.wiley.com/terms-and-conditions) on Wiley Online Library for rules of use; OA articles are governed by the applicable Creative Commons License

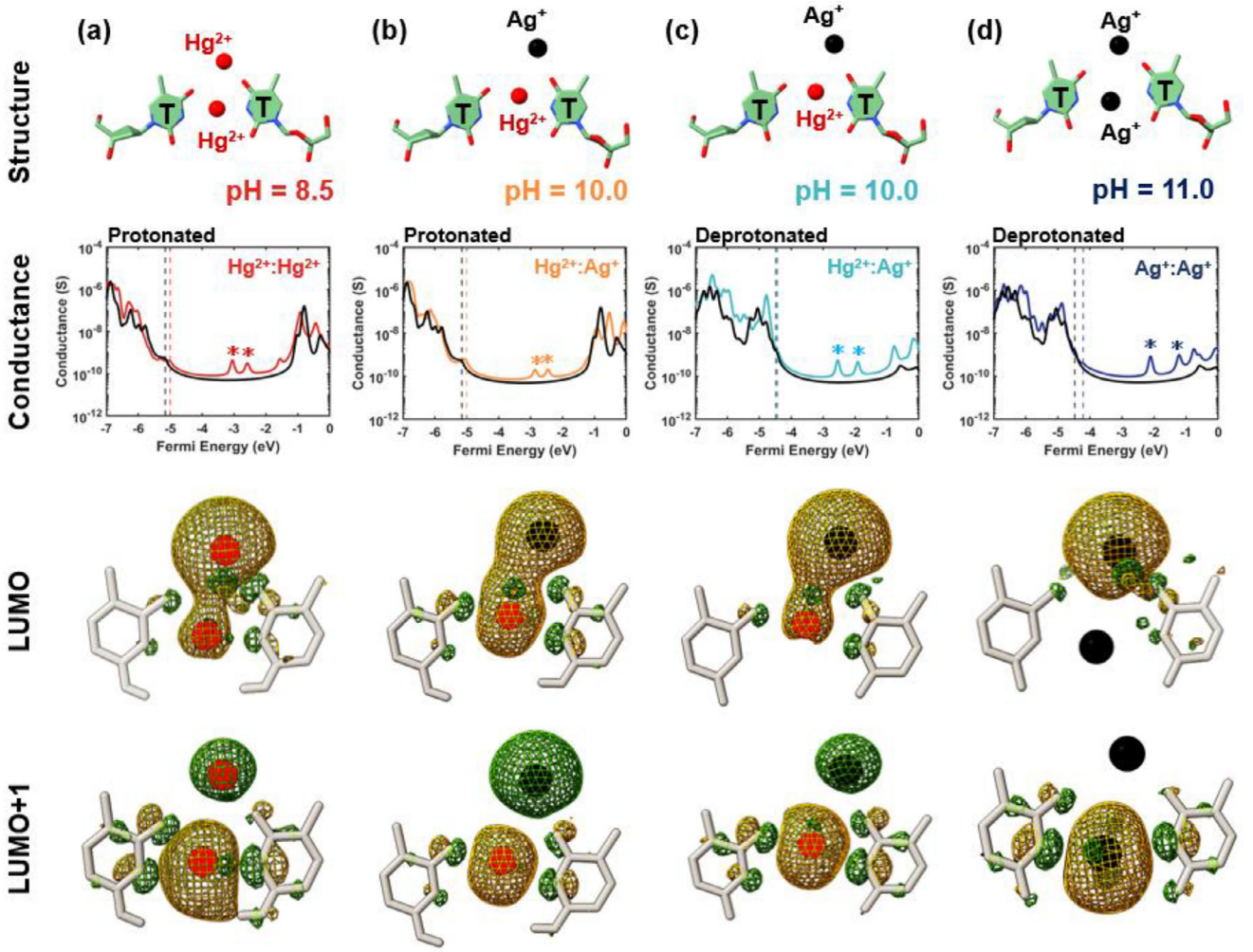


Figure 5. Dinuclear coordination: Computational analysis of charge transport in two ion mmDNA systems at a) pH 8.5 b,c) pH 10.0 d) pH 11.0 are shown. First row: Composition of metal coordination in the T–T base pair. Second row: Conductance variation with various position of Fermi energy in the metal-DNA structures. Third and fourth rows: The first and second LUMO levels are shown (LUMO, LUMO+1) for each case. Wavefunctions with absolute value of more than 0.02 are shown. We have considered two extreme protonated states at pH 10.0 with fully protonated in (b) and fully deprotonated in (c). The black lines in second row show no-metal cases.

tion in the partial charge of the N3-coordinated Hg^{2+}. This results in a highly asymmetric LUMO distribution between the two metals. To more precisely elucidate the broadening of orbitals, we have calculated the probability ($|\psi|^2$) on each metal and DNA as shown in **Table 1**. First, we observe the HOMO to mainly delocalize over the DNA at all pH levels. Next, moving from left to right in Figure 5 (panels a to d), we note the partial charge on N3-coordinated metal to be 1.60 (Hg^{2+}), 1.65 (Hg^{2+}), 1.44 (Hg^{2+}) and 0.49 (Ag^{+}) respectively (see Table 1). The corresponding values of $|\psi|^2$ are 8%, 44%, 9%, and 1% suggesting that the broadening of the lowest unoccupied orbitals between the two metals in a dinuclear coordinated motif is directly proportional to the partial charge of N3-coordinated metal. The broadening is larger when the partial charges of N3- and O4- metals are comparable (see Figure 5b) as reflected in $|\psi|^2$ values. Additionally, it is observed that the contribution of O4-metal to the lowest unoccupied orbital is dominant (84%/86%/92% in Figure 5a,c,d). However, for the protonated heterometallic motif in Figure 5b, the contribution of O4-metal (46%) is comparable to N3-metal (44%). Therefore, in a dinuclear coordinated motif, while the lowest unoccupied orbital predominantly resides on the O4-coordinated metal, the extent of broadening is governed by the nature and partial charge of the N3-coordinated metal.

For the case of Fermi energy being close to the HOMO, we find that conductance is largest for pH 10.0 (see Figure S9a, Supporting Information). The underlying mechanism is elucidated by plotting the five highest-occupied energy levels (see Figure S9b, Supporting Information). These energies lie within a window of 250 meV for pH 10.0 while the energy window is larger in the other three cases as seen in Figure S9b (Supporting Information). The closer energy level spacing implies a stronger conduction pathway for electrons. However, LUMO orbitals are always centered around the metal-coordinated base pairs as shown in Figure S7 (Supporting Information). Finally, we clarify that while the conductance results presented above were calculated between the two 3′ ends of the DNA, we have also calculated the conduc-

© 2025 Wiley-VCH GmbH

16136829, 0, Downloaded from https://onlinelibrary.wiley.com/doi/10.1002/smll.202411518 by University Of Washington, Wiley Online Library on [14/05/2025]. See the Terms and Conditions (https://onlinelibrary.wiley.com/terms-and-conditions) on Wiley Online Library for rules of use; OA articles are governed by the applicable Creative Commons License

Table 1. Probability ($|\Psi|^2$) on DNA, N3- and O4-metal at HOMO (H), LUMO (L) and LUMO+1 (L1) energies. The colored numbers represent significant contribution. All numbers are rounded to the nearest integer.

pH	Orbital	DNA			N3-metal					O4-metal				
	Map	$\|\Psi\|^2$ (in %)			Nature	Charge	$\|\Psi\|^2$ (in %)			Nature	Charge	$\|\Psi\|^2$ (in %)		
	Broadening[b)]	H	L	L1			H	L	L1			H	L	L1
8.5	High	100	8	17	Hg^{2+}	1.60	0	8	73	Hg^{2+}	1.92	0	84	10
10.0	Very High	100	10	7	Hg^{2+}	1.65	0	44	40	Ag^{+}	0.96	0	46	53
10.0[a)]	Low	100	5	19	Hg^{2+}	1.44	0	9	68	Ag^{+}	0.95	0	86	13
11.0[a)]	Very Low	100	7	17	Ag^{+}	0.49	0	1	81	Ag^{+}	0.85	0	92	2

[a)] Deprotonated; [b)] Broadening between N3- and O4- coordinated metals.

tance between the two 5′ ends, and between all atoms at the two ends (see Figure S8, Supporting Information). Our theoretical estimates for the conductance contrast are robust in these cases and the results have been summarized in Table S5 (Supporting Information).

In **Table 2**, we present the summary of computationally estimated conductance modulation ratio at the HOMO and LUMO energy levels due to both single- and two-metal mmDNA. Transport is modeled between the 3′ ends of the DNA in Table 2. The metal-intercalated structures lead to good conductance modulation at HOMO and even better conductance contrast at the LUMO. In particular, the conductance contrast for dinuclear metal pairs increases with pH from 8.85 at the LUMO level at pH 8.5 to 15.9 at pH 11.0. We further note at intermediate pH 10.0, the conductance ratio can be expected to vary between 4 to 11. From a fundamental perspective, our calculations show that the coordination of metal ions adds a new conduction channel in the LUMO. But in most cases, it disrupts the conduction pathway through the nucleobases at the HOMO level due to distortion to accommodate the metal atom. This can be seen in Table 2 and Table S5 (Supporting Information) which demonstrates the robustness of the assertion of different contact configurations. These calculations demonstrate a significant change in conductance as a result of pH-induced mmDNA configuration. While a read-only memory with a high resistance contrast is theoretically possible with DNA,[26,27,61] pathways to create a rewritable memory have remained a challenge. Sequence-based encoding has been developed, though these approaches use a slow sequencing or nanopore readout and have limited ability to re-write bits.[62,63] The method established here informs the ability to build tunable, metalated DNA networks that can compete with current technologies.

We observed different metal coordination at either the N3 or O4 sites of T:T mismatched base pairs due to the neutral-to-alkaline transition and vice versa. Additionally, Liu et al have shown the removal and addition of metal atoms to mismatched DNA base pairs upon application of EDTA at a constant pH.[64] Hence, such metalated DNA motifs offer two types of switching: 1) modulation at a fixed pH by removing and binding metal atoms; and 2) modulation by switching between alkaline and neutral pH to drive transmetalation and generate at least two resistance states.

3. Discussion

In this work, we have demonstrated a metal ion coordination-based method in which one or more transition metal ions can be dynamically positioned inside base pairs to modulate the conductance. We develop a means to carry out pH-based transmetalation within single base pairs without disrupting the topology of the DNA double helix. Using crystallographic analysis, we can solve the structure of the forward and reverse chemical reactions, yielding a fundamental advance both in the determination of structures from self-assembled crystals and in the reconfigurability of DNA-based molecular electronics. We note that the transmetalation observed here does not fully regenerate the starting state—while the alkaline to neutral reconfiguration sees homobimetallic, T:Ag^{+}/Ag^{+}:T fully convert to homobimetallic T:Hg^{2+}/Hg^{2+}:T, the reverse reaction begins with homobimetallic T: Hg^{2+}/Hg^{2+}/T and yields only a single metal, O4 T: Ag^{+}:T base

Table 2. Conductance contrast for mmDNA at HOMO and LUMO levels with 3'- 3' contacts. Green and Yellow rows represent fully protonated and deprotonated states.

PDB ID	pH	Metal Ions	$\frac{G_{no-metal}}{G_{metal}}$ (HOMO, HOMO + 1)	$\frac{G_{metal}}{G_{no-metal}}$ (LUMO)
I. Single Metal Coordinated Motifs				
7TG6	7.0	Hg^{2+}	0.82, 0.74	6.47
7SLG	11.0	Ag^{+}	7.69, 0.73	3.22
II. Dinuclear Coordinated Motifs				
7SM0	8.5	Hg^{2+}, Hg^{2+}	1.35, 0.72	8.85
7SM3	10.0	Hg^{2+}, Ag^{+}	1.06, 0.77	4.04
			1.04, 0.67	10.78
7SM5	11.0	Ag^{+}, Ag^{+}	3.85, 0.64	15.91

© 2025 Wiley-VCH GmbH

16136829, 0, Downloaded from https://onlinelibrary.wiley.com/doi/10.1002/smll.202411518 by University Of Washington, Wiley Online Library on [14/05/2025]. See the Terms and Conditions (https://onlinelibrary.wiley.com/terms-and-conditions) on Wiley Online Library for rules of use; OA articles are governed by the applicable Creative Commons License

pair (Figure 2). With the crystal method developed here, future experiments may be carried out to tune buffer and metal ion concentrations to enable a fully cyclic reconfiguration, which would be key to a memory device. In particular, changing metal concentrations, buffer composition, and pH step size may assist in obtaining a transmetalation loop. Finally, we observe that O4-metal bonds have higher crystallographic B-factors, yielding a wider binding site. Indeed, the structure of single-metal T: Hg^{2+}:T relying on N3-metal bonds showed measurably better conductance than the O4-Ag^{+} analog. We conclude that molecular electronics based on mmDNA will likely require an N3 metal in pyrimidine-pyrimidine base pairs to ensure the planarity of the base pair and good orbital alignment.

Our computational findings reveal that even a single metal atom can induce a LUMO energy level while also modifying the conduction pathway at the HOMO level. While conductance modulation at LUMO is primarily driven by charge transport through the metal atom, at HOMO it is determined by the disruption of the charge transport through DNA caused by the metal atom. From our results, it can be extrapolated that the effect of metal ions will be more pronounced with more metalated bases. For dinuclear coordinated motifs, we observed that the zero-bias conductance contrast at the HOMO is ≈1 to 4, whereas at the LUMO, it ranges from 8 to 16, indicating that metal ion doping predominantly influences the LUMO energy levels (Table 2). This influence is further evidenced by the broadening of LUMO orbitals on metal and metalated base pairs (Figure 5). The interplay between the nature of the coordinated metal and the coordination site plays a crucial role in governing the extent of LUMO orbital broadening (Table 1, Figure 5). While the LUMO orbital primarily resides on O4-coordinated metal, its broadening toward the N3 site is largely dictated by the N3-metal partial charge. In homo-bimetallic coordination, the LUMO orbital extends to the N3 site at pH 8.5 but not at pH 11.0, due to the higher partial charge of coordinated Hg^{2+} compared to Ag^{+}. Deprotonation leads to better conjugation between the bases and the N3-metal, reducing the partial charge of N3-metal. Consequently, the LUMO orbital exhibits less broadening in the deprotonated motif compared to the protonated one (pH 10.0 in Figure 5, Table 1). From our single metal intercalation results, we determined that the nature of coordination significantly affects charge transport, with N3–N3 coordination having a greater impact than O4–O4 (Figure 4). Furthermore, our results highlight the pronounced effect of protonation states on charge transport. During the neutral-to-alkaline pH transition, at intermediate pHs (9.0, 10.0), deprotonation leads to reduced bandgap (≈200 to 500 meV) in comparison to protonated states (Figure 3). Consequently, a large conductance variability is expected at these intermediate pHs, as controlling the protonation states of thymine is difficult. Overall, analysis of the resulting structures reveals that metal ion doping in DNA facilitates advancements in the design of nanoelectronics. Unlike conventional semiconductor technology, it is difficult to dope a DNA structure to enhance its conductivity. The proposed method leverages the pH-dependent activity of modified DNA base pairs to reconfigure Ag^{+} and Hg^{2+} ions, leading to measurable changes in the DNA energy levels and resulting in conductance switching and amplification. The ability to environmentally control the conductance of DNA provides a method for rewriteable memory devices. With appropriate electrical contacts, we anticipate building switchable bits based on pH-controlled transmetalation.

We anticipate that these experiments can serve as a template for time-resolved crystallography in self-assembled DNA crystals to elucidate the kinetics of drug release, molecular switching, and other metal-mediated phenomena. Specifically, we imagine this method will enable the tracking of slow chemical reactions in the porous DNA crystals described here by tracking the loss or gain of heavy atoms by guests in the minor groove, by halogenated strands undergoing strand displacement, or other mmDNA phenomena. Even in systems unable to handle high pH values, the clear and precise placement of silver(I) and mercury(II) allows for specific and measurable changes with subtle pH differences. Indeed, the observation that Hg^{2+} causes orbital broadening to neighboring metals may inform the design of DNA nanowires, where the placement of Hg^{2+} at strategic positions along an axial chain of extended metal arrays may enable electron delocalization and highly efficient conductance. These data suggest that transmetalation may be possible in other nucleobase pairs, with different pKa setpoints tunable to the application or desired buffer conditions. We believe our findings make the prospect of building an array with mmDNA for data storage applications appealing. The transmetalation-driven conductance reconfigurability, which enables modulation of individual mmDNA conductance states within an array, paves the way for a scalable bioelectronic platform capable of performing analog computing–catering to a wide range of edge applications. In summary, the combination of comparable conductance, smaller dimensions, ease of fabrication, extended lifespan, and transmetalation-driven conductance reconfigurability underscores the potential of mmDNA-based technology in the near future.

Supporting Information

Supporting Information is available from the Wiley Online Library or from the author.

Acknowledgements

A.D. and B.L. contributed equally to this work. The authors acknowledge the support of the National Science Foundation to M.P.A., R.S., J.W.C., A.S.B., and J.H. from grant GCR-2317843. This work was further supported by N000141912596 from the Office of Naval Research to R.S. and J.W.C., and DE-SC0007991 to R.S. from the Department of Energy.

Conflict of Interest

The authors declare no conflict of interest.

Data Availability Statement

The data that support the findings of this study are available from the corresponding author upon reasonable request.

Keywords

DNA nanotechnology, metal base pairs, molecular electronics, nanomaterials, transport modeling

© 2025 Wiley-VCH GmbH

16136829, 0, Downloaded from https://onlinelibrary.wiley.com/doi/10.1002/smll.202411518 by University Of Washington, Wiley Online Library on [14/05/2025]. See the Terms and Conditions (https://onlinelibrary.wiley.com/terms-and-conditions) on Wiley Online Library for rules of use; OA articles are governed by the applicable Creative Commons License

Received: November 29, 2024
Revised: April 21, 2025
Published online:

[1] N. C. Seeman, *J. Theor. Biol.* **1982**, *99*, 237.
[2] B. H. Robinson, N. C. Seeman, *Protein Engin Design Sel* **1987**, *1*, 295.
[3] N. R. Kallenbach, R.-I. Ma, N. C. Seeman, *Nature* **1983**, *305*, 829.
[4] N. C. Seeman, *J. Biomol. Struct. Dyn.* **1990**, *8*, 573.
[5] J. P. K. Doye, T. E. Ouldridge, A. A. Louis, F. Romano, P. Sulc, C. Matek, B. E. K. Snodin, L. Rovigatti, J. S. Schreck, R. M. Harrison, W. P. J. Smith, *Phys. Chem. Chem. Phys.* **2013**, *15*, 20395.
[6] E. Winfree, F. Liu, L. A. Wenzler, N. C. Seeman, *Nature* **1998**, *394*, 539.
[7] C. Mao, W. Sun, C. Nadrian, *J. Am. Chem. Soc.* **1999**, *121*, 5437.
[8] P. W. K. Rothemund, *Nature* **2006**, *440*, 297.
[9] G. Tikhomirov, P. Petersen, L. Qian, *Nature* **2017**, *552*, 67.
[10] J. H. Reif, *Natural Computing* **2003**, *2*, 439.
[11] L. Qian, E. Winfree, *Science* **2011**, *332*, 1196.
[12] L. Qian, E. Winfree, J. Bruck, *Nature* **2011**, *475*, 368.
[13] L. Feng, S. H. Park, J. H. Reif, H. Yan, *Angew Chem Intl Ed* **2003**, *42*, 4342.
[14] W. Wang, C. Chen, S. Vecchioni, T. Zhang, C. Wu, Y. P. Ohayon, R. Sha, N. C. Seeman, B. Wei, *Angew Chem Intl Ed.* **2021**, *60*, 25781.
[15] J. Song, Z. Li, P. Wang, T. Meyer, C. Mao, Y. Ke, *Science* **2017**, *357*, aan3377.
[16] S. M. Hart, X. Wang, J. Guo, M. Bathe, G. S. Schlau-Cohen, *J. Phys. Chem. Lett.* **2022**, *13*, 1863.
[17] X. Lan, T. Liu, Z. Wang, A. O. Govorov, H. Yan, Y. Liu, *J. Am. Chem. Soc.* **2018**, *140*, 11763.
[18] G. Posnjak, X. Yin, P. Butler, O. Bienek, M. Dass, S. Lee, I. D. Sharp, T. Liedl, *Science* **2024**, *384*, 781.
[19] X. Dai, Q. Li, A. Aldalbahi, L. Wang, C. Fan, X. Liu, *Nano Lett.* **2020**, *20*, 5604.
[20] D. Porath, N. Lapidot, J. Gomez-Herrero, G. Cuniberti, K. Richter, G. Fagas, *Introduc. Mol Elect.*, (Eds: G. Cuniberti, K. Richter, G. Fagas), Springer, Berlin, Heidelberg **2005**, *680*.
[21] J. Qi, Md. G. Rabbani, S. Edirisinghe, M. P. Anantram, *2011 11th IEEE Intl. Conf. Nanotechnol.*, IEEE, Portland, OR, USA **2011**, 487.
[22] C. H. Adessi, S. Walch, M. P. Anantram, *Phys. Rev. B* **2003**, *67*, 081405.
[23] J. Qi, N. Edirisinghe, M. G. Rabbani, M. P. Anantram, *Phys Rev B Condensed Matter Mater Phys* **2013**, *87*, 1.
[24] J. C. Genereux, J. K. Barton, *Chem. Rev.* **2010**, *110*, 1642.
[25] S. Delaney, J. K. Barton, *J. Org. Chem.* **2003**, *68*, 6475.
[26] A. De, H. Mohammad, Y. Wang, R. Kubendran, A. K. Das, M. P. Anantram, *Sci. Rep.* **2023**, *13*, 6650.
[27] A. De, H. Mohammad, Y. Wang, R. Kubendran, A. K. Das, M. P. Anantram, *2022 IEEE 22nd Intl Conf Nanotechnol (Nano)* **2022**, pp. 385–388.
[28] J. M. Artés, Y. Li, J. Qi, M. P. Anantram, J. Hihath, *Nat. Commun.* **2015**, *6*, 8870.
[29] S. Bag, S. Mogurampelly, W. A. G. Iii, P. K. Maiti, *Nanoscale* **2016**, *8*, 16044.
[30] H. Mohammad, B. Demir, C. Akin, B. Luan, J. Hihath, E. E. Oren, M. P. Anantram, *Nanoscale Horiz.* **2021**, *6*, 651.
[31] L. Xiang, J. L. Palma, Y. Li, V. Mujica, M. A. Ratner, N. Tao, *Nat. Commun.* **2017**, *8*, 14471.
[32] E. Braun, Y. Eichen, U. Sivan, G. Ben-Yoseph, *Nature* **1998**, *391*, 775.
[33] A. Stern, G. Eidelshtein, R. Zhuravel, G. I. Livshits, D. Rotem, A. Kotlyar, D. Porath, *Adv. Mater.* **2018**, *30*, 1800433.
[34] J. Liu, Y. Geng, E. Pound, S. Gyawali, J. R. Ashton, J. Hickey, A. T. Woolley, J. N. Harb, *ACS Nano* **2011**, *5*, 2240.
[35] A. Michelson, A. Subramanian, K. Kisslinger, N. Tiwale, S. Xiang, E. Shen, J. S. Kahn, D. Nykypanchuk, H. Yan, C.-Y. Nam, O. Gang, *Science Adv* **2024**, *10*, adl0604.
[36] N. Fardian-Melamed, G. Eidelshtein, D. Rotem, A. Kotlyar, D. Porath, *Adv. Mater.* **2019**, *31*, 1902816.
[37] G. L. Eichhorn, Y. A. Shin, *J. Am. Chem. Soc.* **1968**, *90*, 7323.
[38] Y.-G. Gao, M. Sriram, *A. H. Wang-J. Nucleic Acids Res.* **1993**, *21*, 4093.
[39] P. Aich, S. L. Labiuk, L. W. Tari, L. J. T. Delbaere, W. J. Roesler, K. J. Falk, R. P. Steer, J. S. Lee, *J. Mol. Biol.* **1999**, *294*, 477.
[40] K. Tanaka, A. Tengeiji, T. Kato, N. Toyama, M. Shionoya, *Science* **2003**, *299*, 1212.
[41] Y. Miyake, H. Togashi, M. Tashiro, H. Yamaguchi, S. Oda, M. Kudo, Y. Tanaka, Y. Kondo, R. Sawa, T. Fujimoto, T. Machinami, A. Ono, *J. Am. Chem. Soc.* **2006**, *128*, 2172.
[42] A. Ono, S. Cao, H. Togashi, M. Tashiro, T. Fujimoto, T. Machinami, S. Oda, Y. Miyake, I. Okamoto, Y. Tanaka, *Chem. Commun.* **2008**, *39*, 4825.
[43] Z. V. Reveguk, E. V. Khoroshilov, A. V. Sharkov, V. A. Pomogaev, A. A. Buglak, A. I. Kononov, *J. Phys. Chem. B* **2024**, *128*, 4377.
[44] O. P. Schmidt, G. Mata, N. W. Luedtke, *J. Am. Chem. Soc.* **2016**, *138*, 14733.
[45] E. Bethur, R. Guha, Z. Zhao, B. B. Katz, P. D. Ashby, H. Zeng, S. M. Copp, *ACS Nano* **2024**, *18*, 3002.
[46] B. Lu, S. Vecchioni, Y. P. Ohayon, J. W. Canary, R. Sha, *Biophys. J.* **2022**, *121*, 4759.
[47] S. Vecchioni, B. Lu, W. Livernois, Y. P. Ohayon, J. B. Yoder, C.-F. Yang, K. Woloszyn, W. Bernfeld, M. P. Anantram, J. W. Canary, W. A. Hendrickson, L. J. Rothschild, C. Mao, S. J. Wind, N. C. Seeman, R. Sha, *Adv. Mater.* **2023**, *35*, 2210938.
[48] B. Lu, Y. P. Ohayon, K. Woloszyn, C.-F. Yang, J. B. Yoder, L. J. Rothschild, S. J. Wind, W. A. Hendrickson, C. Mao, N. C. Seeman, J. W. Canary, R. Sha, S. Vecchioni, *J. Am. Chem. Soc.* **2023**, *145*, 17945.
[49] B. Lu, S. Vecchioni, Y. P. Ohayon, K. Woloszyn, T. Markus, C. Mao, N. C. Seeman, J. W. Canary, R. Sha, *Small* **2022**, *19*, 2205830.
[50] B. Lu, S. Vecchioni, Y. P. Ohayon, R. Sha, K. Woloszyn, B. Yang, C. Mao, N. C. Seeman, *ACS Nano* **2021**, *15*, 16788.
[51] J. Zheng, J. J. Birktoft, Y. I. Chen, T. Wang, R. Sha, P. E. Constantinou, S. L. Ginell, C. Mao, N. C. Seeman, *Nature* **2009**, *461*, 74.
[52] S. Vecchioni, B. Lu, J. Janowski, K. Woloszyn, N. Jonoska, N. C. Seeman, C. Mao, Y. P. R. Ohayon, *Small* **2023**, *19*, 2206511.
[53] B. Lu, K. Woloszyn, Y. P. Ohayon, B. Yang, C. Zhang, C. Mao, N. C. Seeman, S. Vecchioni, R. Sha, *Angew. Chem. Intl. Ed.* **2022**, *62*, 202213451.
[54] Y. Li, J. M. Artés, B. Demir, S. Gokce, H. M. Mohammad, M. Alangari, M. P. Anantram, E. E. Oren, J. Hihath, *Nat. Nanotechnol.* **2018**, *13*, 1167.
[55] D. T. Cromer, J. T. Waber, *Acta Cryst D Biol Cryst* **1965**, *18*, 104.
[56] G. Brändén, R. Neutze, *Science* **2021**, *373*, aba0954.
[57] A. Das, O. Gerlits, J. M. Parks, P. Langan, A. Kovalevsky, W. T. Heller, *Structure* **2015**, *23*, 2331.
[58] S. Nehzati, A. O. Summers, N. V. Dolgova, J. Zhu, D. Sokaras, T. Kroll, I. J. Pickering, G. N. George, *Inorg. Chem.* **2021**, *60*, 7442.
[59] J. Sebera, J. Burda, M. Straka, A. Ono, C. Kojima, Y. Tanaka, V. Sychrovský, *Chem. Eur. J.* **2013**, *19*, 9884.
[60] J. Kondo, T. Yamada, C. Hirose, I. Okamoto, Y. Tanaka, A. Ono, *Angew. Chem. Intl. Ed.* **2014**, *53*, 2385.
[61] S. R. Patil, H. Mohammad, V. Chawda, N. Sinha, R. K. Singh, J. Qi, M. P. Anantram, *ACS Applied Nano Mater* **2021**, *4*, 10029.
[62] C. Pan, S. K. Tabatabaei, S. M. H. Tabatabaei Yazdi, A. G. Hernandez, C. M. Schroeder, O. Milenkovic, *Nat. Commun.* **2022**, *13*, 2984.
[63] K. Chen, J. Zhu, F. Bošković, U. F. Keyser, *Nano Lett.* **2020**, *20*, 3754.
[64] S. Liu, G. H. Clever, Y. Takezawa, M. Kaneko, K. Tanaka, X. Guo, M. Shionoya, *Angew. Chem. Intl. Ed.* **2011**, *50*, 8886.

© 2025 Wiley-VCH GmbH

16136829, 0, Downloaded from https://onlinelibrary.wiley.com/doi/10.1002/smll.202411518 by University Of Washington, Wiley Online Library on [14/05/2025]. See the Terms and Conditions (https://onlinelibrary.wiley.com/terms-and-conditions) on Wiley Online Library for rules of use; OA articles are governed by the applicable Creative Commons License